

Information Content of Hierarchical n -Point Polytope Functions for Quantifying and Reconstructing Disordered Systems

Pei-En Chen¹, Wenxiang Xu^{2, 3, *}, Yi Ren^{1, *}, and Yang Jiao^{2, 4, *}

¹ Mechanical Engineering, Arizona State University, Tempe AZ 85287, USA

² Materials Science and Engineering, Arizona State University, Tempe AZ 85287, USA

³ College of Mechanics and Materials, Hohai University, Nanjing 211100, P.R. China

⁴ Materials Science and Engineering, Arizona State University, Tempe AZ 85287, USA

* Corresponding author, E-mail: xwxfat@gmail.com (W.X.), yang.jiao.2@asu.edu (Y. J.) and yiren@asu.edu (Y. R.)

Abstract

Disordered systems are ubiquitous in physical, biological and material sciences. Examples include liquid and glassy states of condensed matter, colloids, granular materials, porous media, composites, alloys, packings of cells in avian retina and tumor spheroids, to name but a few. A comprehensive understanding of such disordered systems requires, as the first step, systematic quantification, modeling and representation of the underlying complex configurations and microstructure, which is generally very challenging to achieve. Recently, we introduce a set of hierarchical statistical microstructural descriptors, i.e., the “ n -point polytope functions” P_n , which are derived from the standard n -point correlation functions S_n , and successively include higher-order n -point statistics of the morphological features of interest in a concise, explainable, and expressive manner. Here we investigate the information content of the P_n functions via optimization-based realization rendering. This is achieved by successively incorporating higher order P_n functions up to $n = 8$ and quantitatively assessing the accuracy of the reconstructed systems via un-constrained statistical morphological descriptors (e.g., the lineal-path function). We examine a wide spectrum of representative random systems with distinct geometrical and topological features. We find that generally, successively incorporating higher order P_n functions, and thus, the higher-order morphological information encoded in these descriptors, leads to superior accuracy of the reconstructions. However, incorporating more P_n functions into the reconstruction also significantly increases the complexity and roughness of the associated energy landscape for the underlying stochastic optimization, making it difficult to convergence numerically.

Key words: disordered system, information content, correlation functions, stochastic reconstruction

1. Introduction

Disordered systems such as liquid and glassy states of condensed matter [1, 2], colloids [3], granular materials [4, 5], porous media [6, 7], composites [8-10], alloys [11], biopolymer networks [12-15], packings of cells in avian retina [16] and tumor spheroids [17, 18], are ubiquitous in physical, biological and material sciences. The recently discovered disordered low-dimensional quantum materials [19] have demonstrated great potentials for a wide spectrum of device applications. A comprehensive understanding of such disordered systems requires, as the first step, systematic quantification, modeling and representation of the underlying complex configurations and microstructure, which is generally very challenging to achieve. One challenge involves the *in situ* non-destructive characterization of the 3D configuration or microstructure containing key features of interest for these systems on multiple length scales. This challenge has been partially addressed by the development and successful application of advanced non-destructive *in situ* imaging techniques, such as x-ray micro-computed tomography (μ CT) [20, 21]. The second challenge involves the development of efficient mathematical frameworks and computational tools for quantitative representation, modeling and reconstruction of such complex disordered systems.

In general, it is notoriously difficult, if not impossible, to derive a mathematically concise yet complete quantification and representation of a disordered system, due to the intrinsic large number of degrees of freedom required to uniquely specify such a system. For example, to uniquely define a crystal structure, one only needs to specify the basis and a set of translation vectors; while to define the structure of glass, the positions of the atoms are required. Recently, a variety of novel approaches have been developed to address the challenges for quantifying disordered systems. In particular, intensive research activities have been devoted to devising *reduced-dimension statistical* quantification and representation based on either complete 3D or lower dimensional structural data set [9, 22-41], and to devising the associated realization rendering methods based on the reduced-dimension representations [42-69]. Examples of established reduced-dimension representation schemes include random field models, statistical descriptor-based representations, and abstract image-based decompositions obtained via machine-learning, to name but a few. Among the descriptor-based representations, a recently developed framework for Hierarchical Materials Informatics, based on complete 2-point statistics and its lower dimensional projections [70-72], can directly yield accurate estimates of properties of a wide class of engineering materials [59, 73-80] and thus, has been incorporated into various integrated computational material design frameworks.

One of the most widely-used descriptor-based set of representations includes the standard n -point correlation (or probability) functions S_n , which encode the occurrence probability of specific n -point configurations in the system [8, 81-83]. The complete set of S_n with $n = 1, 2, 3, \dots \infty$ provides a complete quantitative microstructure representation, and thus, determines the physical properties of the system under consideration. It has been shown that even the lower-order function S_2 can be employed to model a wide spectrum of distinct disordered systems, such as heterogeneous materials [84-91]. In general, it is very challenging to utilize S_n with $n \geq 3$, for which one needs to enumerate all distinct n -point configurations and efficiently compute and store their probability of occurrence. The resulting statistical data sets are typically comparable or even larger in size than the original number of degrees of freedom for the system. It has been shown that two-point statistics alone might not be sufficient to represent certain complex microstructures [92-95]. An alternative approach is to employ non-standard lower-order correlation functions such as the cluster functions [96, 97] or surface functions [98, 99], which encode partial higher-order n -point statistics. This method is very effective in capturing specific morphological features (e.g., clustering) [52] but is typically computationally extensive.

Recently, we develop a set of hierarchical statistical morphological descriptors, called the “*n-point polytope functions*” P_n [100], which can provide concise, expressive, and explainable quantification and representation of a wide spectrum of disordered systems. In particular, the polytope functions successively include higher-order n -point statistics of the features of interest in the system, and can be directly computed from multi-modal imaging data, including x-ray tomographic radiographs, optical/SEM/TEM micrographs, and EBSD color maps for quantification of different features of interest. In addition, efficient computational tools to directly extract these statistical descriptors from imaging data has been developed, and the utility of functions for quantifying complex heterogeneous materials and microstructural evolution has been successfully demonstrated [100].

In this work, we systematically investigate the information content of the P_n functions via optimization-based realization rendering. This is achieved by successively incorporating higher order P_n functions up to $n = 8$ to generate material realizations corresponding to the specified set of function, and quantitatively assessing the accuracy of the reconstructed systems via un-constrained statistical morphological descriptors (e.g., the lineal-path function). We examine a wide spectrum of representative random systems with distinct geometrical and topological features, including representative crystalline and disordered particle particles, Poisson distribution of particles, microstructures of concrete and interpenetrating metal-ceramic composites. We find that generally, successively incorporating higher order P_n functions, and thus, the higher-order morphological information encoded in these descriptors, leads to superior accuracy of the reconstructions. However, incorporating more P_n functions into the

reconstruction also significantly increases the complexity and roughness of the associated energy landscape for the underlying stochastic optimization, making it difficult to converge numerically. These results suggest that the P_n functions can provide a superior quantification and representation of complex disordered systems.

2. The n-Point Polytope Functions P_n and Realization Rendering via Stochastic Optimization

2.1. Definition of the n-point polytope functions P_n

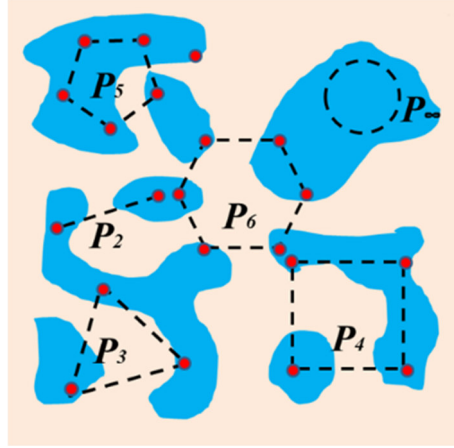


Fig. 1: Schematic illustration of stochastic events contributing to the P_n functions in the case of regular polygons.

Without loss of generality, we consider the n -point polytope functions P_n defined for a heterogeneous material (represented as a continuous random field) in which the different structural features are segmented and grouped into different “phases”. A simple example is a composite microstructure contains a “matrix phase” and a “particle phase”, see Fig. 1. Note that a many-particle system can be easily mapped to a binary random field, e.g., by placing a solid sphere at the center of each particle. The definition of P_n is then given as follows:

$P_n(r) \equiv$ *Probability that all of the n vertices of a randomly selected regular n -point polytope with edge length r fall into the phase of interest.*

Two sets of the P_n functions can be derived based on this definition. The first set involves *n -point regular polygons*, for which the vertex (edge) number n can take any positive integer values; and in the limit $n \rightarrow \infty$, the shape becomes a circle (in this limiting case, the quantity r is the radius of the circle, instead of the edge length). We note that the *n -point polygonal functions* can be computed from both 2D slices and full 3D realizations. The other set involves 3D polyhedra whose edges are of the same length. Only a small number of 3D polyhedra satisfy this condition, including the five *Platonic solids* (i.e., the regular

polyhedra: tetrahedron, octahedron, dodecahedron, icosahedron, and cube) and the thirteen *Archimedean solids* (i.e., the semi-regular polyhedra) [101]. Importantly, we note it is clear from the definition that the P_n function is a subset of the corresponding full S_n function. In particular, the former only contains statistics associated with a special subset of the n -point configurations corresponding to a regular n -polytope with different sizes; while the latter encodes statistical information of all n -point configurations. In the case of $n = 2$, the 2-point polytope function P_2 is identical to the standard 2-point correlation function S_2 .

Figure 1 schematically illustrates the stochastic events that contribute to the P_n functions in the case of regular polygons. For $r = 0$, the polygon reduces to a single point, and $P_n(r=0)$ gives the volume fraction ϕ of the phase of interest (i.e., the probability a randomly selected point falling into the phase of interest). For finite r values, $P_n(r)$ provides n -point spatial correlations in the phase (feature) of interest. For very large r values (e.g., $r \rightarrow \infty$), the probabilities of finding the vertices in the phase of interest are almost independent of one another, thus, we have $P_n(r \rightarrow \infty) \approx \phi^n$, where ϕ is the volume fraction of the phase of interest in the system. These asymptotic behaviors allow us to introduce a convenient re-scaled form of the P_n functions, i.e.,

$$f_n(r) = \left[P_n(r) - \phi^n \right] / \left[\phi - \phi^n \right] \quad (1)$$

with $f_n(r=0) = 1$ and $f_n(r \rightarrow \infty) = 0$. Finally, we note that one can define “cross-correlation” polytope functions, by requiring a subset of the vertices falling into different phases (features) in the microstructure. In this paper, we will mainly focus on the “auto” polytope functions defined with 2D polygons, in which all of the vertices of the polygons fall into the same phase of interest.

2.2. Extracting P_n functions from imaging data

The probability-based definition of the P_n functions allow us to easily compute these function from microstructural data, including both 2D images and 3D digital representations of the material microstructure. For example, in order to compute the value of $P_n(r)$ with $r = r^*$, the following procedure is used:

- (i) A regular n -polytope (e.g., a n -polygon) with edge length r^* is generated;
- (ii) This n -polygon is then placed in the material microstructure with randomly selected center location and random orientation, for M times (see Fig. 2a);
- (iii) Each time the polygon is placed in the system, its vertices is checked to see if they all fall into the phase of interest (i.e., a “success” event); and the total number of success event M_s out of a total of M trials is subsequently recorded;

- (iv) The rate of success $P_n(r=r^*) = Ms/M$ is computed, which is the probability that a randomly selected n -polygon having all its vertices fall into the phase of interest.

This procedure is repeated for different r values to compute the full $P_n(r)$ function.

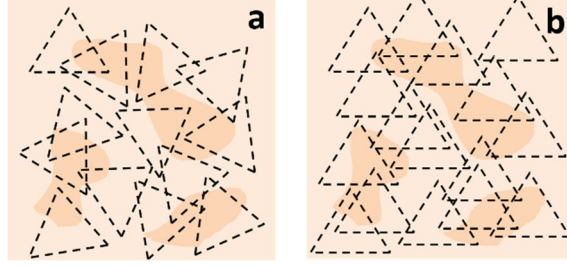


Fig. 2: Schematic illustration of different sampling templates for computing P_n functions (in the case of $n=3$) from images: (a) Isotropic sampling, in which both the location and orientation of the polygon template are randomly selected. (b) Directional sampling, in which only the location of the template is randomly selected.

We note that for a digitized representation of a material microstructure (i.e., an image), a point falls into the phase of interest if it falls into a pixel (or voxel in 3D) of that phase. Therefore, the edge length of the pixel/voxel defines the smallest distance in the system and provides a natural unit for measuring the distance. In addition, besides placing the polytope template with random orientations (i.e., isotropic sampling), one can fix the orientation of the polytopes while placing them at randomly selected locations, see Fig. 2b. We refer to this later case as “directional sampling”.

2.3. Realization rendering via stochastic optimization

In this section, we briefly describe the Yeung-Torquato (YT) procedure for rendering material realizations via stochastic optimization [102, 103]. In the YT procedure, the reconstruction problem is formulated as an “energy” minimization problem, with the energy functional E defined as follows

$$E = \sum_n \sum_{\beta} \sum_r \left[P_n^{\beta}(r) - \bar{P}_n^{\beta}(r) \right]^2 \quad (2)$$

where $\bar{P}_n^{\beta}(r)$ is a target polytope function of order n along direction β and $P_n^{\beta}(r)$ is the corresponding function associated with a trial realization. In this work, we incorporated P_n functions up to $n = 8$. The simulated annealing method [104, 105] is usually employed to solve the aforementioned minimization problem. Specifically, starting from an initial trial realization (i.e., *old* microstructure) which contains a fixed number of voxels for each phase consistent with the volume fraction of that phase, two randomly selected voxels associated with different phases are exchanged to generate a *new* trial realization. The

associated P_n functions are sampled from the new trial realization and the associated energy is evaluated, which determines whether the new trial realization should be accepted or not via the probability:

$$p_{acc}(old \rightarrow new) = \min \left\{ 1, \exp\left(\frac{E_{old}}{T}\right) / \exp\left(\frac{E_{new}}{T}\right) \right\} \quad (3)$$

where T is a virtual temperature that is chosen to be high initially and slowly decreases according to a cooling schedule [48, 51]. The above process is repeated until E is smaller than a prescribed tolerance, which we choose to be 10^{-6} here. Generally, several hundred thousand trials need to be made to achieve such a small tolerance, for which we consider convergence is achieved.

An important step in the reconstruction process is to efficiently compute the correlation functions from the trial microstructure, which is especially crucial for the reconstruction of large-scale 3D realizations. The key idea is to only compute the change in the P_n functions due to the switch of randomly selected pixel pair, instead of re-compute the functions from scratch. This can be implemented by identifying the polygonal sampling templates that have been affected by the pixel exchange and recomputing the contributions from these templates after the pixel exchange. We note that when n gets larger, the number of affected n -polygonal templates also increases rapidly. Since our focus in this work is to investigate the information content of the hierarchical set of P_n functions using relatively small 2D systems (e.g., ~ 100 by 100 pixels), we afford to directly recompute the P_n functions from new trial realizations without significantly increasing the computational cost.

3. Information Content of P_n Functions via Realization Rendering

In this section, we investigate the information content of the P_n functions using a variety of heterogeneous systems, including ordered and disordered particle packings respectively representing crystalline and liquid state of matters, overlapping particles with a Poisson distribution of particle centers, interpreting microstructure of metal-ceramic composite, and concrete microstructure. This is achieved by incorporating additional P_n functions of successively higher orders into the realization reconstructions, starting with the fundamental two-point function P_2 (or equivalently S_2). The accuracy of the reconstructed realizations are subsequently accessed using statistical descriptors that are not used in the reconstruction, such as the lineal-path function $L(r)$ [52, 106], which provides the probability that a randomly placed line segment of length r entirely lying in the phase of interest. In particular, the lineal-path function $L(r)$ will be computed from both the original system and the reconstructed realization. The accuracy metric ψ , defined as the sum of the absolute differences of these two functions over all r values, will also be computed, i.e.,

$$\Psi = \sum_r |L(r) - L^*(r)| \quad (4)$$

where $L(r)$ and $L^*(r)$ are respectively computed from the reconstructed realization and the original system. The level of accuracy of the realizations, quantified via ψ , reflects the statistical information encoded in the P_n functions. For example, higher accuracy indicates essential additional structural information is encoded in the newly added functions. In the following realization rendering cases, the size of the reconstructed system is 80 by 80 pixels without further elaboration, and periodic boundary conditions are employed.

3.1 Ordered packing of congruent spheres

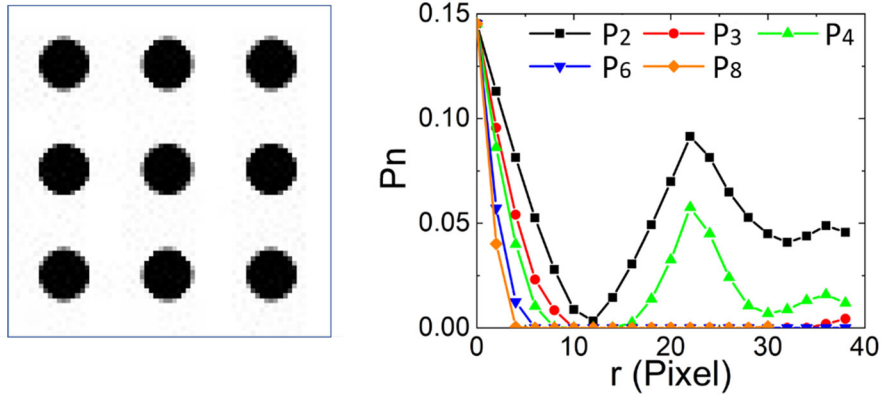


Fig. 3: A simple 2D crystalline packing of congruent spheres on a square lattice (left) and the associated P_n function for the particle phase (right).

We begin with a simple 2D crystalline packing of congruent spheres on a square lattice (see Fig. 3a). The volume fraction of the particle phase is $\phi = 0.14$. It can be clearly seen from Fig. 3b that both the P_2 (i.e., S_2) and P_4 functions exhibit strong oscillations, which is a manifestation of the underlying 4-fold symmetry of the structure. The other P_n functions (i.e., $n=3, 6, 8$) do not exhibit significant oscillation beyond an initial decay, reflecting the fact that the system is composed of compact particles as building blocks, but does not possess strong n -point correlations on large length scales.

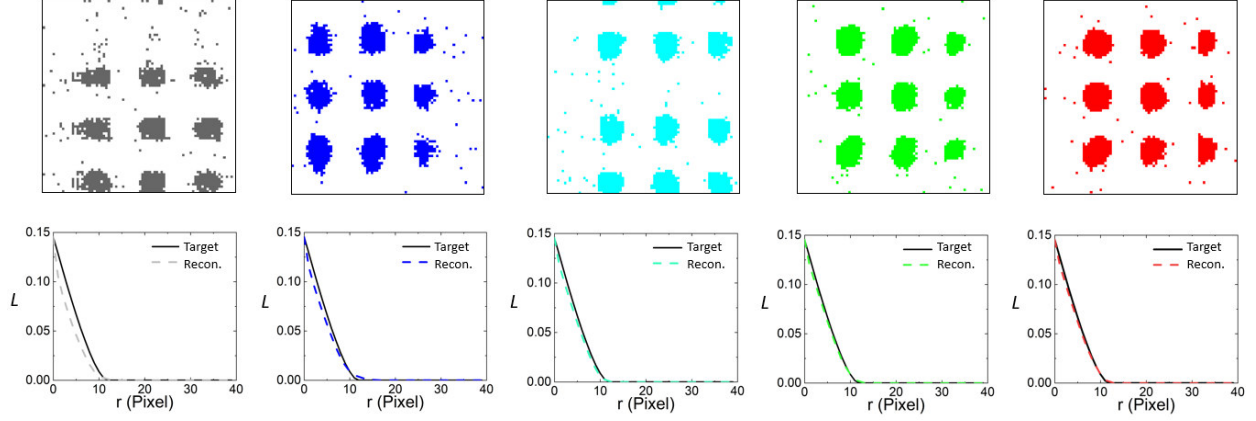


Fig. 4: Realizations of 2D crystalline packing of congruent spheres on a square lattice (upper panels) and the associated lineal-path functions (lower panels) obtained via stochastic reconstruction by successively incorporating higher-order P_n functions. The functions incorporated from left to right are respectively: P_2 , $\{P_2, P_3\}$, $\{P_2, P_3, P_4\}$, $\{P_2, P_3, P_4, P_6\}$, and $\{P_2, P_3, P_4, P_6, P_8\}$.

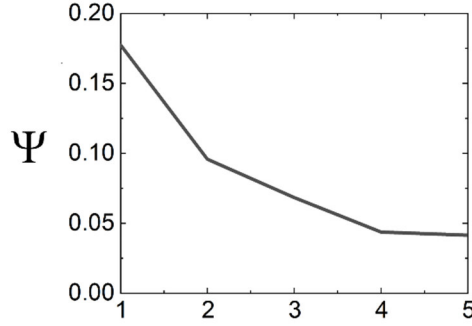


Fig. 5: Accuracy metric ψ defined in Eq. (4) associated with reconstructions incorporating different sets of P_n functions. The horizontal axis indicates the number of functions incorporated in the reconstruction.

Figure 4 shows the realizations (upper panels) obtained via stochastic reconstruction by successively incorporating higher-order P_n functions. The functions incorporated from left to right are respectively: P_2 , $\{P_2, P_3\}$, $\{P_2, P_3, P_4\}$, $\{P_2, P_3, P_4, P_6\}$, and $\{P_2, P_3, P_4, P_6, P_8\}$. It can be seen that the spatial arrangement of the particles on the square lattice is reproduced in all cases. This is because the structural information for the highly ordered 4-fold symmetric arrangement is already captured by the lowest order function P_2 , which is further reinforced by incorporating P_4 . Interestingly, the shape of the particle is improved due to incorporation of additional functions, i.e., P_3 , P_6 , and P_8 . This is consistent with information content of these functions, i.e., P_3 , P_6 , and P_8 functions do not possess long-range oscillations and thus, only encode information on the morphology of the particles. The lineal-path functions L are computed from the reconstructed realizations and compared to that of the original system (see Fig. 4, lower panels). It can be seen as higher order P_n functions are successively incorporated, the L function of the reconstructed

realizations matches the original system better. This is consistent with the quantification using accuracy metric shown in Fig. 5.

3.2 Disordered packing of congruent spheres

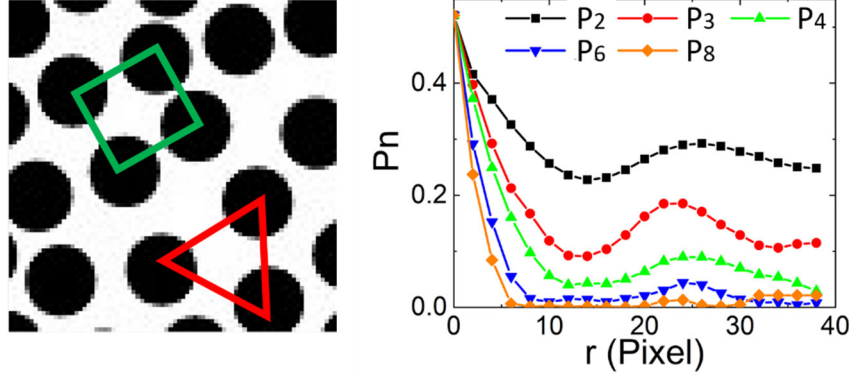


Fig. 6: A 2D disordered packing of congruent hard spheres generated via Monte Carlo simulations (left) and the associated P_n function for the particle phase (right).

Fig. 6 shows the quantification of a 2D microstructure composed of equal-sized hard spheres in a matrix [48], i.e., a packing (see Fig. 6, left panel). The sphere packing is generated using Monte Carlo simulations [101]. The P_n functions for the particle phase with $n=2, 3, 4, 6$ and 8 are shown in Fig. 6 right panel. Similar to the crystalline packing case discussed in Sec. 3.1, all P_n functions initially decay from the volume fraction $\phi=0.48$ as r increases from 0. The positions of the first minimum in the P_n functions for small n values roughly correspond to the linear size of the particle (~ 12 pixels). After the initial decay, all P_n functions studied here except for $n=8$ exhibit relatively significant oscillations and the first peaks in different P_n functions occur at approximately the same r values. These oscillations respectively indicate strong pair, triangle, square and hexagonal correlations on different length scales in the system. In Fig. 6, we illustrate examples of such correlations, which are all associated with the mean nearest neighbor separate distance, i.e., the distance associated with the first peak in P_2 . These correlations result from the tendency for the particles to self-organize at high densities.

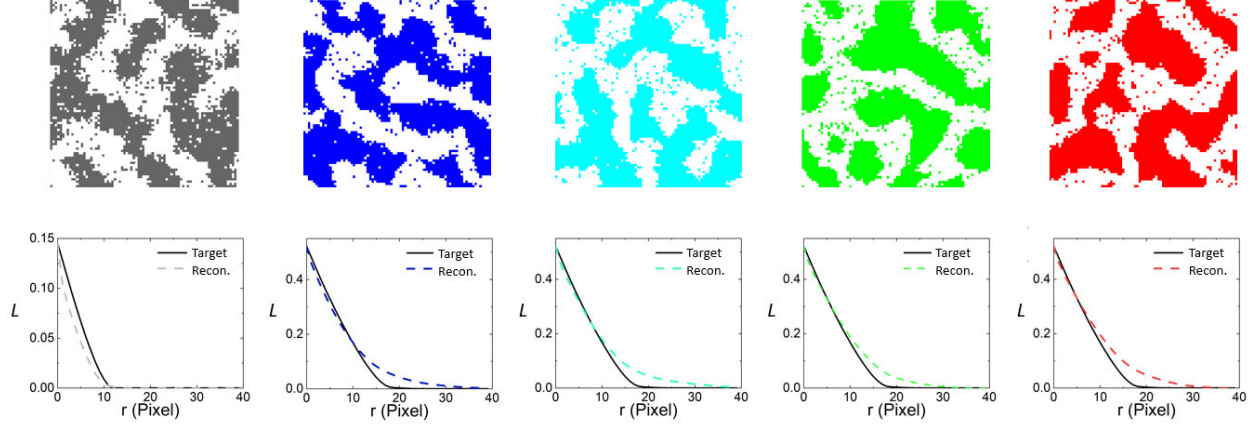


Fig. 7: Realizations of disordered packing of congruent hard spheres (upper panels) and the associated lineal-path functions (lower panels) obtained via stochastic reconstruction by successively incorporating higher-order P_n functions. The functions incorporated from left to right are respectively: P_2 , $\{P_2, P_3\}$, $\{P_2, P_3, P_4\}$, $\{P_2, P_3, P_4, P_6\}$, and $\{P_2, P_3, P_4, P_6, P_8\}$.

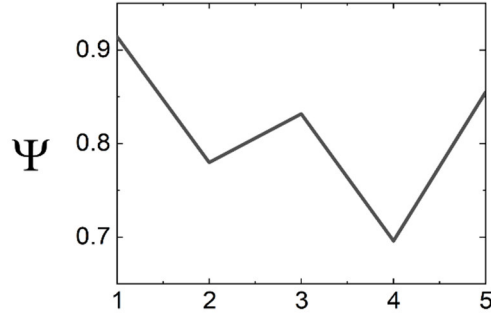


Fig. 8: Accuracy metric ψ defined in Eq. (4) associated with reconstructions incorporating different sets of P_n functions. The horizontal axis indicates the number of functions incorporated in the reconstruction.

Figure 7 shows the realizations (upper panels) obtained via stochastic reconstruction by successively incorporating higher-order P_n functions. The functions incorporated from left to right are respectively: P_2 , $\{P_2, P_3\}$, $\{P_2, P_3, P_4\}$, $\{P_2, P_3, P_4, P_6\}$, and $\{P_2, P_3, P_4, P_6, P_8\}$. It can be seen that in all reconstructions, the connectivity of the particle phase has been significantly overestimated. In particular, instead of reproducing individual compact particles, a single connected phase with a characteristic ligament size comparable to the sphere diameter is produced. The strong oscillation in the correlation functions is realized by the inter-ligament spacing and correlations. This is because the particle volume fraction $\phi=0.48$ is close to percolation [107] [108]. These results also indicate that the P_n functions (up to $n = 8$) do not encode topological connectedness information. On the other hand, it has been shown that incorporating cluster functions [41, 52] can lead to significantly improved reconstructions capturing the connectivity information. The lineal-path functions L also are computed from the reconstructed

realizations and compared to that of the original system (see Fig. 7 lower panels). Since L is sensitive to clustering, which is overestimated in all realizations, successively incorporating higher-order P_n functions does not lead successively more accurate reconstruction. Instead, the more complex energy landscape associated with higher-order P_n functions might lead to slower convergence of the reconstruction, and higher probability that the system gets stuck in a shallow local minimum. This is consistent with the quantification using accuracy metric shown in Fig. 8.

3.3 Overlapping congruent spheres

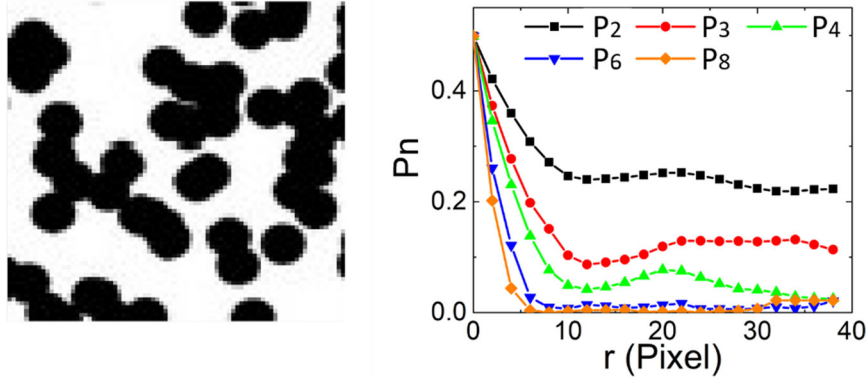


Fig. 9: A 2D disordered packing of congruent overlapping spheres with a Poisson distribution of the particle centers (left) and the associated P_n function for the particle phase (right).

Fig. 9 shows the quantification of a 2D microstructure composed of equal-sized overlapping spheres in a matrix [48] (see Fig. 9, left panel). The spheres are randomly placed in the matrix without any built-in spatial correlations. Fig. 9 right panel shows the P_n functions for the particle phase with $n=2, 3, 4, 6$ and 8 . Similar to the previous systems, all P_n functions initially decay from the volume fraction $\phi=0.47$ as r increases from 0. After the initial decay, the P_n functions are virtually flat, indicating that the particles possess no spatial correlations of any symmetry on any length scales beyond the diameter of the particles. We note that for the totally random overlapping sphere system, the P_n functions possess the analytical expression $P_n(r) = \exp[-\rho v_n(r; R)]$, where ρ is the number density of the spheres in the system (i.e., number of spheres per unit volume) and $v_n(r; R)$ is the volume of the union of n spheres with radius R with centers placed at the vertices of a n -polytope with edge length r .

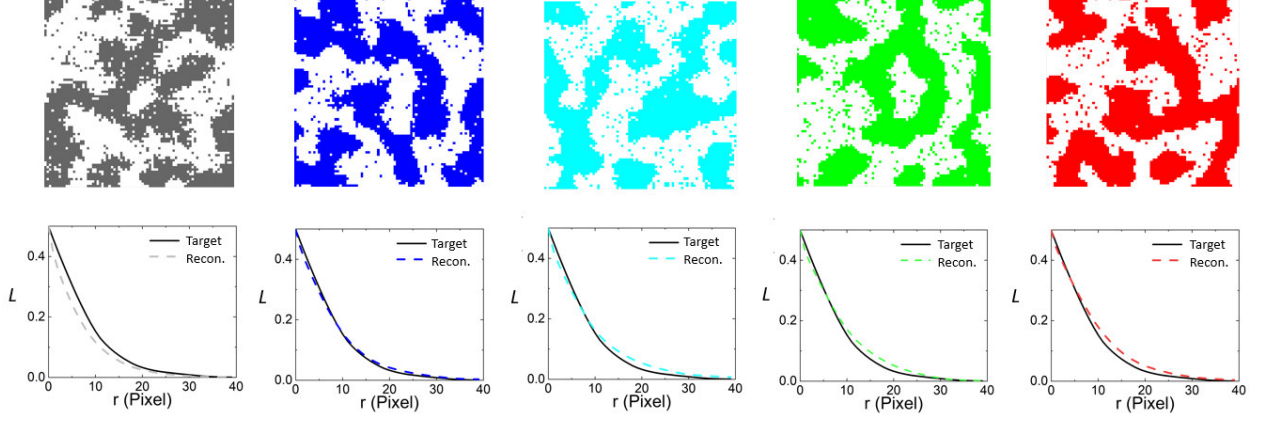


Fig. 10: Realizations of overlapping sphere packing (upper panels) and the associated lineal-path functions (lower panels) obtained via stochastic reconstruction by successively incorporating higher-order P_n functions. The functions incorporated from left to right are respectively: P_2 , $\{P_2, P_3\}$, $\{P_2, P_3, P_4\}$, $\{P_2, P_3, P_4, P_6\}$, and $\{P_2, P_3, P_4, P_6, P_8\}$.

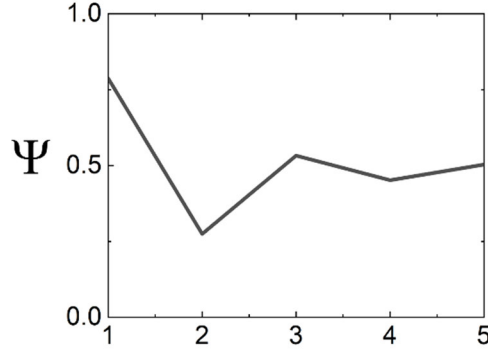


Fig. 11: Accuracy metric ψ defined in Eq. (4) associated with reconstructions incorporating different sets of P_n functions. The horizontal axis indicates the number of functions incorporated in the reconstruction.

Fig. 10 shows the realizations (upper panels) obtained via stochastic reconstruction by successively incorporating higher-order P_n functions. The functions incorporated from left to right are respectively: P_2 , $\{P_2, P_3\}$, $\{P_2, P_3, P_4\}$, $\{P_2, P_3, P_4, P_6\}$, and $\{P_2, P_3, P_4, P_6, P_8\}$. In all the reconstructions, the connectivity of the particle phase has been correctly reproduced, as the overlapping particles in the original system form a single connected phase, in contrast to the hard sphere packing case. Since all the P_n functions contains no essential information beyond the particle diameter (~ 12 pixels), incorporating these functions does not lead to improvement of the reconstruction accuracy for the overlapping sphere system. This is consistent with the quantification using accuracy metric shown in Fig. 11.

3.4 Concrete microstructure

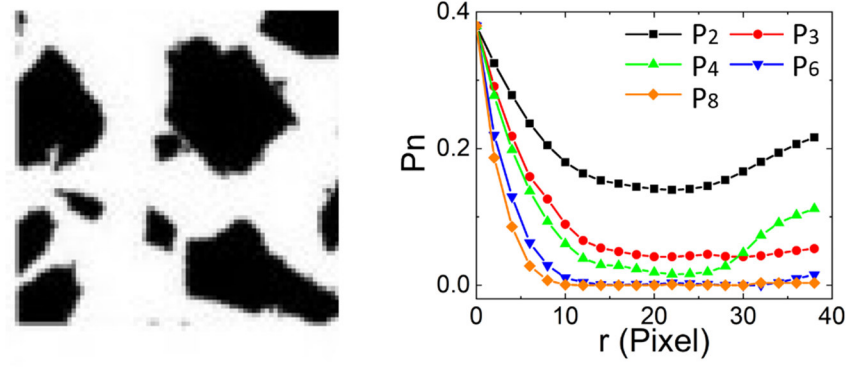


Fig. 12: A 2D slice of a concrete microstructure in which the cement paste is shown in white and the rocks are shown in black (left) and the associated P_n function for the rock phase (right).

Fig. 12 shows the quantification of a 2D concrete microstructure composed of reinforcement rocks (shown in black) and the cement paste (shown in white) [52] (see Fig. 12, left panel). The rock particles possess complex polygonal morphologies and a wide size distribution. Fig. 12 right panel shows the P_n functions for the rock phase with $n=2, 3, 4, 6$ and 8 . All P_n functions initially decay from the volume fraction $\phi=0.38$ as r increases from 0. The r value associated with the first minimum in the functions provides the average particle size in the system, i.e., ~ 20 pixels. After the initial decay, the lower-order P_n functions (e.g., $n \leq 4$) increase, reflecting the spatial correlations resulted from the mutual exclusion effects of the rock particles. The correlations are much weaker compared those in hard-sphere systems, mainly due to the anisotropy and size polydispersity of the rock particles.

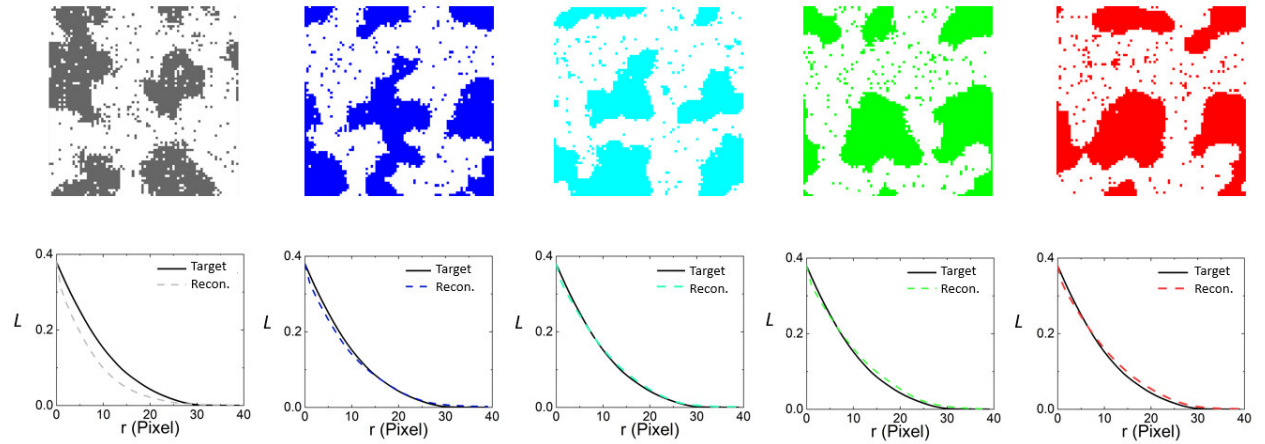


Fig. 13: Realizations of concrete microstructures (upper panels) and the associated lineal-path functions (lower panels) obtained via stochastic reconstruction by successively incorporating higher-order P_n functions. The functions incorporated from left to right are respectively: P_2 , $\{P_2, P_3\}$, $\{P_2, P_3, P_4\}$, $\{P_2, P_3, P_4, P_6\}$, and $\{P_2, P_3, P_4, P_6, P_8\}$.

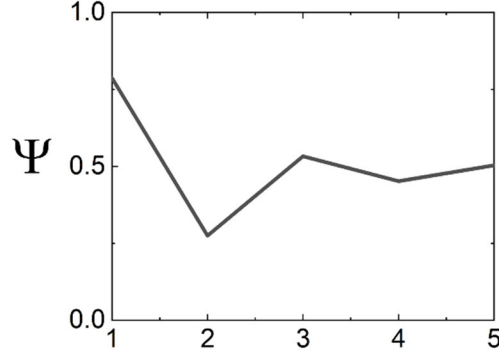


Fig. 14: Accuracy metric ψ defined in Eq. (4) associated with reconstructions incorporating different sets of P_n functions. The horizontal axis indicates the number of functions incorporated in the reconstruction.

Fig. 13 shows the realizations (upper panels) obtained via stochastic reconstruction by successively incorporating higher-order P_n functions. The functions incorporated from left to right are respectively: P_2 , $\{P_2, P_3\}$, $\{P_2, P_3, P_4\}$, $\{P_2, P_3, P_4, P_6\}$, and $\{P_2, P_3, P_4, P_6, P_8\}$. In the reconstructions, individual rock particles can be clearly distinguished. As higher-order P_n functions are successively incorporated, the shape and morphology of the rock particles are improved. This can be seen both from visual inspection of the reconstructed realizations and the quantitative comparison of the lineal-path functions (Fig. 13, right lower panels). In the case that a larger number of P_n functions are incorporated, the complexity of energy landscape increases dramatically, leading to very slow convergence of the reconstruction. This also leads to the slight increase of ψ shown in Fig. 14.

3.5 Interpenetrating metal-ceramic composite

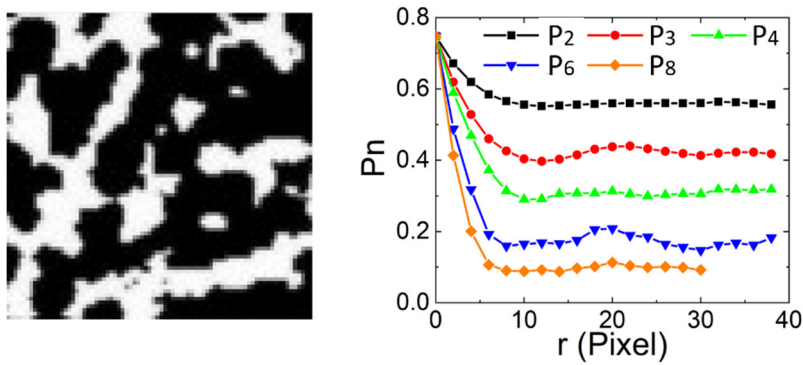


Fig. 15: A 2D slice of an interpenetrating microstructure of a metal-ceramic composite composed of the boron-carbide phase (black) and the aluminum phase (white) (left) and the associated P_n function for the boron-carbide (ceramic) phase (right).

Fig. 15 shows the quantification of a 2D an interpenetrating metal-ceramic composite composed of the boron-carbide phase (shown in black) and the aluminum phase (shown in white) [51] (see Fig. 9a). This system contains “ligaments” of similar width instead of “particles”, and possesses connected material phase, in contrast to the hard particle packings. Fig. 15 right panel shows the P_n functions for the ceramic phase with $n=2, 3, 4, 6$ and 8 . Similar to the previous systems, all P_n functions initially decay from the volume fraction $\varphi=0.76$ as r increases from 0. The r value associated with the first minimum in the functions provides the average ligament width in the system, i.e., ~ 10 pixels. After the initial decay, the P_n functions exhibit weak oscillations for small and intermediate r values, characterizing the exclusion effects between the ligaments.

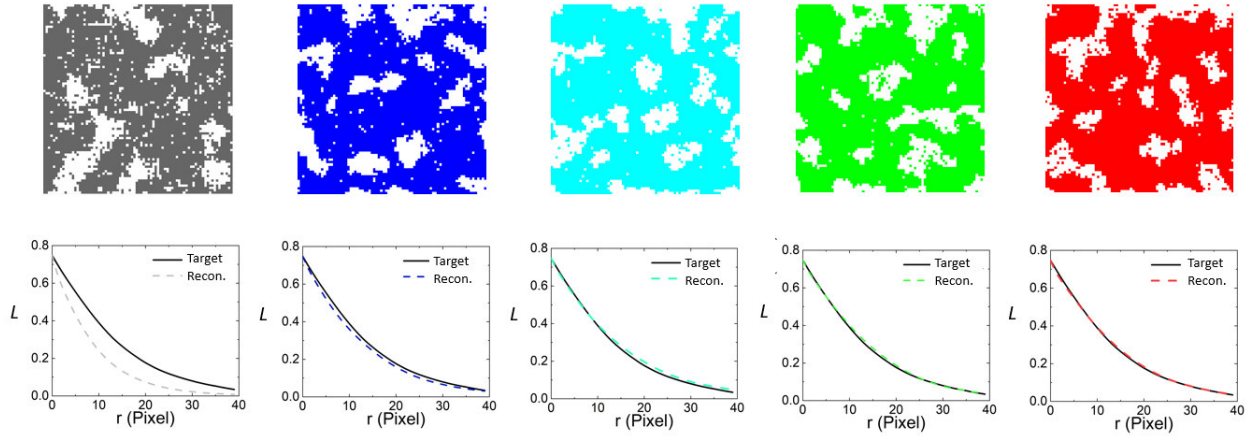


Fig. 16: Realizations of the interpenetrating microstructure (upper panels) and the associated lineal-path functions (lower panels) obtained via stochastic reconstruction by successively incorporating higher-order P_n functions. The functions incorporated from left to right are respectively: P_2 , $\{P_2, P_3\}$, $\{P_2, P_3, P_4\}$, $\{P_2, P_3, P_4, P_6\}$, and $\{P_2, P_3, P_4, P_6, P_8\}$.

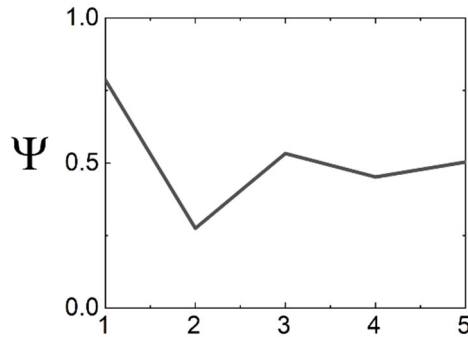


Fig. 17: Accuracy metric ψ defined in Eq. (4) associated with reconstructions incorporating different sets of P_n functions. The horizontal axis indicates the number of functions incorporated in the reconstruction.

Fig. 16 shows the realizations (upper panels) obtained via stochastic reconstruction by successively incorporating higher-order P_n functions. The functions incorporated from left to right are respectively: P_2 , $\{P_2, P_3\}$, $\{P_2, P_3, P_4\}$, $\{P_2, P_3, P_4, P_6\}$, and $\{P_2, P_3, P_4, P_6, P_8\}$. In all the reconstructions, the morphology and connectivity of both the ceramic and metallic phases have been very well reproduced. As can be seen from the comparison of the lineal-path functions (Fig. 16, lower panels) and the accuracy metric ψ (see Fig. 17), including higher-order P_n functions leads to successively improved reconstructions. This indicates that the additional morphological information encoded in higher-order P_n functions has been efficiently utilized in the reconstructions. We note that it is relatively easier for the reconstruction algorithm to converge to a realization with connected phase at high volume fractions, as such realizations are more degenerate [94, 95]. Therefore, it is common that better reconstruction accuracy can be achieved for systems where the phase of interest (i.e., the ceramic phase) is connected.

4. Conclusions and Discussion

In this work, we employ stochastic realization reconstruction to probe the level of statistical morphological information contained in a recently introduced set of hierarchical statistical microstructural descriptors, i.e., the “ n -point polytope functions” P_n . The $P_n(r)$ function provides the probability of finding a set of n points sitting at the vertices a regular n -polytope of edge length r in the phase of interest, and thus, is a subset of the corresponding standard n -point correlation function S_n . In particular, P_n functions up to $n = 8$ were successively incorporated into the Yeong-Torquato reconstruction procedure and the accuracy of the reconstructed systems was quantitatively assessing via the lineal-path function, which provides “linear clustering” information. We examined a wide spectrum of representative random systems with distinct geometrical and topological features, including representative crystalline and disordered particle particles, Poisson distribution of particles, microstructures of concrete and interpenetrating metal-ceramic composites.

We found that generally, successively incorporating higher order P_n functions which encodes essential higher-order morphological information leads to superior accuracy of the reconstructions. However, incorporating more P_n functions into the reconstruction also significantly increases the complexity and roughness of the associated energy landscape for the underlying stochastic optimization, making it difficult to convergence numerically. Another observation is that the P_n functions (up to $n = 8$ studied here) appear to be not sensitive to topological connectedness information. This was evidenced by the significant overestimation of the clustering in the reconstruction of disordered packings of hard spheres near percolation point. These examples indicate that for certain complex systems, successively incorporating higher order correlation functions in a linear fashion might not be the best practice, as one

can significantly increase the computational cost without incorporating too much useful additional morphological information. An alternative approach in such cases is to utilize non-conventional functions (e.g., those encoding clustering information) or to employ machine learning techniques to identify and extract crucial higher order correlations that leapfrog unnecessary computation of all the P_n functions [109-111].

Acknowledgement

This work is supported by ACS Petroleum Research Fund under Grant No. 56474-DNI10 (Program manager: Dr. Burtrand Lee).

References:

1. Binder, K. and W. Kob, *Glassy materials and disordered solids: An introduction to their statistical mechanics*. 2011: World scientific.
2. Hansen, J.-P. and I.R. McDonald, *Theory of simple liquids*. 1990: Elsevier.
3. Chaikin, P.M., T.C. Lubensky, and T.A. Witten, *Principles of condensed matter physics*. Vol. 10. 1995: Cambridge university press Cambridge.
4. Ristow, G.H., *Pattern formation in granular materials*. 2000: Springer Science & Business Media.
5. Jaeger, H.M., S.R. Nagel, and R.P. Behringer, *Granular solids, liquids, and gases*. Reviews of modern physics, 1996. **68**(4): p. 1259.
6. Sahimi, M., *Flow and transport in porous media and fractured rock: from classical methods to modern approaches*. 2011: John Wiley & Sons.
7. Sahimi, M., *Flow phenomena in rocks: from continuum models to fractals, percolation, cellular automata, and simulated annealing*. Reviews of modern physics, 1993. **65**(4): p. 1393.
8. Torquato, S., *Random heterogeneous materials: microstructure and macroscopic properties*. Vol. 16. 2013: Springer Science & Business Media.
9. Brandon, D. and W.D. Kaplan, *Microstructural characterization of materials*. 2013: John Wiley & Sons.
10. Sahimi, M., *Heterogeneous Materials I: Linear transport and optical properties*. Vol. 22. 2003: Springer Science & Business Media.
11. Porter, D.A., K.E. Easterling, and M. Sherif, *Phase transformations in metals and alloys (Revised Reprint)*. 2009: CRC press.
12. Nan, H., L. Liang, G. Chen, L. Liu, R. Liu, and Y. Jiao, *Realizations of highly heterogeneous collagen networks via stochastic reconstruction for micromechanical analysis of tumor cell invasion*. Physical Review E, 2018. **97**(3): p. 033311.
13. Liang, L., C. Jones, S. Chen, B. Sun, and Y. Jiao, *Heterogeneous force network in 3D cellularized collagen networks*. Physical biology, 2016. **13**(6): p. 066001.
14. Jones, C.A.R., L. Liang, D. Lin, Y. Jiao, and B. Sun, *The spatial-temporal characteristics of type I collagen-based extracellular matrix*. Soft Matter, 2014. **10**(44): p. 8855-8863.
15. Jiao, Y. and S. Torquato, *Quantitative characterization of the microstructure and transport properties of biopolymer networks*. Physical biology, 2012. **9**(3): p. 036009.
16. Jiao, Y., T. Lau, H. Hatzikirou, M. Meyer-Hermann, J.C. Corbo, and S. Torquato, *Avian photoreceptor patterns represent a disordered hyperuniform solution to a multiscale packing problem*. Physical Review E, 2014. **89**(2): p. 022721.
17. Jiao, Y. and S. Torquato, *Evolution and morphology of microenvironment-enhanced malignancy of three-dimensional invasive solid tumors*. Physical Review E, 2013. **87**(5): p. 052707.

18. Jiao, Y., H. Berman, T.-R. Kiehl, and S. Torquato, *Spatial organization and correlations of cell nuclei in brain tumors*. PloS one, 2011. **6**(11).
19. Zheng, Y., L. Liu, H. Nan, Z.-X. Shen, G. Zhang, D. Chen, L. He, W. Xu, M. Chen, and Y. Jiao, *Enhanced Electronic Transport in Disordered Hyperuniform Two-Dimensional Amorphous Silica*. arXiv preprint arXiv:1911.03066, 2019.
20. Williams, J., K. Yazzie, E. Padilla, N. Chawla, X. Xiao, and F. De Carlo, *Understanding fatigue crack growth in aluminum alloys by in situ X-ray synchrotron tomography*. International Journal of Fatigue, 2013. **57**: p. 79-85.
21. Singh, S., J. Williams, M. Lin, X. Xiao, F. De Carlo, and N. Chawla, *In situ investigation of high humidity stress corrosion cracking of 7075 aluminum alloy by three-dimensional (3D) X-ray synchrotron tomography*. Materials Research Letters, 2014. **2**(4): p. 217-220.
22. Gueguen, Y. and J. Dienes, *Transport properties of rocks from statistics and percolation*. Mathematical geology, 1989. **21**(1): p. 1-13.
23. Frary, M.E. and C.A. Schuh, *Correlation-space description of the percolation transition in composite microstructures*. Physical Review E, 2007. **76**(4): p. 041108.
24. Groeber, M., S. Ghosh, M.D. Uchic, and D.M. Dimiduk, *A framework for automated analysis and simulation of 3d polycrystalline microstructures.: Part 1: Statistical characterization*. Acta Materialia, 2008. **56**(6): p. 1257-1273.
25. Niezgoda, S., D. Fullwood, and S. Kalidindi, *Delineation of the space of 2-point correlations in a composite material system*. Acta Materialia, 2008. **56**(18): p. 5285-5292.
26. Jiang, L., N. Chawla, M. Pacheco, and V. Noveski, *Three-dimensional (3D) microstructural characterization and quantification of reflow porosity in Sn-rich alloy/copper joints by X-ray tomography*. Materials Characterization, 2011. **62**(10): p. 970-975.
27. Kalidindi, S.R., S.R. Niezgoda, and A.A. Salem, *Microstructure informatics using higher-order statistics and efficient data-mining protocols*. Jom, 2011. **63**(4): p. 34-41.
28. Sosa, J., S. Koduri, V. Dixit, P. Collins, S. Niezgoda, S. Kalidindi, and H. Fraser, *Application of Novel Techniques to the Three-Dimensional Characterization of Microstructural Features in α + β Titanium Alloys*. Minerals, Metals and Materials Society/AIME, 420 Commonwealth Dr., P. O. Box 430 Warrendale PA 15086 United States.[np]. Feb, 2011.
29. Wilding, S.E. and D.T. Fullwood, *Clustering metrics for two-phase composites*. Computational Materials Science, 2011. **50**(7): p. 2262-2272.
30. Callahan, P.G., *Quantitative characterization and comparison of precipitate and grain shape in Ni-base superalloys using moment invariants*. 2012, Carnegie Mellon University.
31. Cecen, A., E. Wargo, A. Hanna, D. Turner, S. Kalidindi, and E. Kumbur, *3-D microstructure analysis of fuel cell materials: spatial distributions of tortuosity, void size and diffusivity*. Journal of The Electrochemical Society, 2012. **159**(3): p. B299-B307.
32. Salem, A., D. Turner, D. Satko, J. Shaffer, S. Niezgoda, and S. Kalidindi. *Quantifying Ti-6 Al-4 V Bimodal Microstructure Using Microstructure Informatics*. in *AIP Conference Proceedings*. 2012. American Institute of Physics, Ste. 1 NO 1 Melville NY 11747-4502 United States.
33. Wang, M., J. Williams, L. Jiang, F. De Carlo, T. Jing, and N. Chawla, *Three Dimensional (3D) Microstructural Characterization and Quantitative Analysis of Solidified Microstructures in Magnesium-Based Alloys*. Metallography, Microstructure, and Analysis, 2012. **1**(1): p. 7-13.
34. Niezgoda, S.R. and J. Glover, *Unsupervised learning for efficient texture estimation from limited discrete orientation data*. Metallurgical and Materials Transactions A, 2013. **44**(11): p. 4891-4905.
35. Niezgoda, S.R., A.K. Kanjarla, and S.R. Kalidindi, *Novel microstructure quantification framework for databasing, visualization, and analysis of microstructure data*. Integrating Materials and Manufacturing Innovation, 2013. **2**(1): p. 1-27.
36. Ratanaphan, S., Y. Yoon, and G.S. Rohrer, *The five parameter grain boundary character distribution of polycrystalline silicon*. Journal of Materials Science, 2014. **49**(14): p. 4938-4945.

37. Hardin, T., T. Ruggles, D. Koch, S. Niezgoda, D. Fullwood, and E. Homer, *Analysis of traction-free assumption in high-resolution EBSD measurements*. Journal of microscopy, 2015. **260**(1): p. 73-85.
38. Cecen, A., T. Fast, and S.R. Kalidindi, *Versatile algorithms for the computation of 2-point spatial correlations in quantifying material structure*. Integrating Materials and Manufacturing Innovation, 2016. **5**(1): p. 1-15.
39. Choudhury, A., Y.C. Yabansu, S.R. Kalidindi, and A. Dennstedt, *Quantification and classification of microstructures in ternary eutectic alloys using 2-point spatial correlations and principal component analyses*. Acta Materialia, 2016. **110**: p. 131-141.
40. Ma, Z. and S. Torquato, *Precise algorithms to compute surface correlation functions of two-phase heterogeneous media and their applications*. Physical Review E, 2018. **98**(1): p. 013307.
41. Malmir, H., M. Sahimi, and Y. Jiao, *Higher-order correlation functions in disordered media: Computational algorithms and application to two-phase heterogeneous materials*. Physical Review E, 2018. **98**(6): p. 063317.
42. Roberts, A.P., *Statistical reconstruction of three-dimensional porous media from two-dimensional images*. Physical Review E, 1997. **56**(3): p. 3203.
43. Pilotti, M., *Reconstruction of clastic porous media*. Transport in Porous Media, 2000. **41**(3): p. 359-364.
44. Saylor, D.M., J. Fridy, B.S. El-Dasher, K.-Y. Jung, and A.D. Rollett, *Statistically representative three-dimensional microstructures based on orthogonal observation sections*. Metallurgical and Materials Transactions A, 2004. **35**(7): p. 1969-1979.
45. Okabe, H. and M.J. Blunt, *Pore space reconstruction using multiple-point statistics*. Journal of Petroleum Science and Engineering, 2005. **46**(1): p. 121-137.
46. Sundararaghavan, V. and N. Zabaras, *Classification and reconstruction of three-dimensional microstructures using support vector machines*. Computational Materials Science, 2005. **32**(2): p. 223-239.
47. Brahme, A., M. Alvi, D. Saylor, J. Fridy, and A. Rollett, *3D reconstruction of microstructure in a commercial purity aluminum*. Scripta Materialia, 2006. **55**(1): p. 75-80.
48. Jiao, Y., F. Stillinger, and S. Torquato, *Modeling heterogeneous materials via two-point correlation functions: Basic principles*. Physical Review E, 2007. **76**(3): p. 031110.
49. Fullwood, D., S. Kalidindi, S. Niezgoda, A. Fast, and N. Hampson, *Gradient-based microstructure reconstructions from distributions using fast Fourier transforms*. Materials Science and Engineering: A, 2008. **494**(1): p. 68-72.
50. Fullwood, D.T., S.R. Niezgoda, and S.R. Kalidindi, *Microstructure reconstructions from 2-point statistics using phase-recovery algorithms*. Acta Materialia, 2008. **56**(5): p. 942-948.
51. Jiao, Y., F. Stillinger, and S. Torquato, *Modeling heterogeneous materials via two-point correlation functions. II. Algorithmic details and applications*. Physical Review E, 2008. **77**(3): p. 031135.
52. Jiao, Y., F. Stillinger, and S. Torquato, *A superior descriptor of random textures and its predictive capacity*. Proceedings of the National Academy of Sciences, 2009. **106**(42): p. 17634-17639.
53. Hajizadeh, A., A. Safekordi, and F.A. Farhadpour, *A multiple-point statistics algorithm for 3D pore space reconstruction from 2D images*. Advances in water Resources, 2011. **34**(10): p. 1256-1267.
54. Blacklock, M., H. Bale, M. Begley, and B. Cox, *Generating virtual textile composite specimens using statistical data from micro-computed tomography: 1D tow representations for the Binary Model*. Journal of the Mechanics and Physics of Solids, 2012. **60**(3): p. 451-470.
55. Rinaldi, R.G., M. Blacklock, H. Bale, M.R. Begley, and B.N. Cox, *Generating virtual textile composite specimens using statistical data from micro-computed tomography: 3D tow representations*. Journal of the Mechanics and Physics of Solids, 2012. **60**(8): p. 1561-1581.

56. Tahmasebi, P. and M. Sahimi, *Cross-correlation function for accurate reconstruction of heterogeneous media*. Physical review letters, 2013. **110**(7): p. 078002.
57. Xu, H., M.S. Greene, H. Deng, D. Dikin, C. Brinson, W.K. Liu, C. Burkhart, G. Papakonstantopoulos, M. Poldneff, and W. Chen, *Stochastic reassembly strategy for managing information complexity in heterogeneous materials analysis and design*. Journal of Mechanical Design, 2013. **135**(10): p. 101010.
58. Gerke, K.M., M.V. Karsanina, R.V. Vasilyev, and D. Mallants, *Improving pattern reconstruction using directional correlation functions*. EPL (Europhysics Letters), 2014. **106**(6): p. 66002.
59. Xu, H., Y. Li, C. Brinson, and W. Chen, *A Descriptor-Based Design Methodology for Developing Heterogeneous Microstructural Materials System*. Journal of Mechanical Design, 2014. **136**(5): p. 051007.
60. Gerke, K.M. and M.V. Karsanina, *Improving stochastic reconstructions by weighting correlation functions in an objective function*. EPL (Europhysics Letters), 2015. **111**(5): p. 56002.
61. Liu, X. and V. Shapiro, *Random heterogeneous materials via texture synthesis*. Computational Materials Science, 2015. **99**: p. 177-189.
62. Bostanabad, R., A.T. Bui, W. Xie, D.W. Apley, and W. Chen, *Stochastic microstructure characterization and reconstruction via supervised learning*. Acta Materialia, 2016. **103**: p. 89-102.
63. Turner, D.M. and S.R. Kalidindi, *Statistical construction of 3-D microstructures from 2-D exemplars collected on oblique sections*. Acta Materialia, 2016. **102**: p. 136-148.
64. Karsanina, M.V. and K.M. Gerke, *Hierarchical Optimization: Fast and Robust Multiscale Stochastic Reconstructions with Rescaled Correlation Functions*. Physical review letters, 2018. **121**(26): p. 265501.
65. Feng, J., Q. Teng, X. He, and X. Wu, *Accelerating multi-point statistics reconstruction method for porous media via deep learning*. Acta Materialia, 2018. **159**: p. 296-308.
66. Li, H., N. Chawla, and Y. Jiao, *Reconstruction of heterogeneous materials via stochastic optimization of limited-angle X-ray tomographic projections*. Scripta Materialia, 2014. **86**: p. 48-51.
67. Li, H., S. Kaira, J. Mertens, N. Chawla, and Y. Jiao, *Accurate Stochastic Reconstruction of Heterogeneous Microstructures by Limited X-ray Tomographic Projections*. Journal of microscopy, 2016. **264**: p. 339.
68. Li, H., S. Singh, S. Kaira, J. Mertens, J.J. Williams, N. Chawla, and Y. Jiao, *Microstructural Quantification and Property Prediction Using Limited X-ray Tomography Data*. JOM, 2016. **68**: p. 2288.
69. Kamrava, S., M. Sahimi, and P. Tahmasebi, *Quantifying accuracy of stochastic methods of reconstructing complex materials by deep learning*. Physical Review E, 2020. **101**(4): p. 043301.
70. Kalidindi, S.R., *Hierarchical Materials Informatics: Novel Analytics for Materials Data*. 2015: Elsevier.
71. Kalidindi, S.R., J.A. Gomberg, Z.T. Trautt, and C.A. Becker, *Application of data science tools to quantify and distinguish between structures and models in molecular dynamics datasets*. Nanotechnology, 2015. **26**(34): p. 344006.
72. Steinmetz, P., Y.C. Yabansu, J. Hötzer, M. Jainta, B. Nestler, and S.R. Kalidindi, *Analytics for microstructure datasets produced by phase-field simulations*. Acta Materialia, 2016. **103**: p. 192-203.
73. Fullwood, D.T., S.R. Niezgod, B.L. Adams, and S.R. Kalidindi, *Microstructure sensitive design for performance optimization*. Progress in Materials Science, 2010. **55**(6): p. 477-562.
74. Jain, A., J.R. Errington, and T.M. Truskett, *Dimensionality and design of isotropic interactions that stabilize honeycomb, square, simple cubic, and diamond lattices*. Physical Review X, 2014. **4**(3): p. 031049.

75. Sharma, V., C. Wang, R.G. Lorenzini, R. Ma, Q. Zhu, D.W. Sinkovits, G. Pilania, A.R. Oganov, S. Kumar, and G.A. Sotzing, *Rational design of all organic polymer dielectrics*. Nature communications, 2014. **5**.
76. Baldwin, A.F., T.D. Huan, R. Ma, A. Mannodi-Kanakkithodi, M. Tefferi, N. Katz, Y. Cao, R. Ramprasad, and G.A. Sotzing, *Rational Design of Organotin Polyesters*. Macromolecules, 2015. **48**(8): p. 2422-2428.
77. Gupta, A., A. Cecen, S. Goyal, A.K. Singh, and S.R. Kalidindi, *Structure–property linkages using a data science approach: Application to a non-metallic inclusion/steel composite system*. Acta Materialia, 2015. **91**: p. 239-254.
78. Kaczmarowski, A., S. Yang, I. Szlufarska, and D. Morgan, *Genetic algorithm optimization of defect clusters in crystalline materials*. Computational Materials Science, 2015. **98**: p. 234-244.
79. Xu, H., R. Liu, A. Choudhary, and W. Chen, *A Machine Learning-Based Design Representation Method for Designing Heterogeneous Microstructures*. Journal of Mechanical Design, 2015. **137**(5): p. 051403.
80. Kirklin, S., J.E. Saal, V.I. Hegde, and C. Wolverton, *High-throughput computational search for strengthening precipitates in alloys*. Acta Materialia, 2016. **102**: p. 125-135.
81. Torquato, S. and G. Stell, *Microstructure of two-phase random media. I. The n-point probability functions*. The Journal of Chemical Physics, 1982. **77**(4): p. 2071-2077.
82. Torquato, S. and G. Stell, *Microstructure of two-phase random media. III. The n-point matrix probability functions for fully penetrable spheres*. The Journal of chemical physics, 1983. **79**(3): p. 1505-1510.
83. Torquato, S. and G. Stell, *Microstructure of two-phase random media. V. The n-point matrix probability functions for impenetrable spheres*. The Journal of chemical physics, 1985. **82**(2): p. 980-987.
84. Jiao, Y., E. Padilla, and N. Chawla, *Modeling and predicting microstructure evolution in lead/tin alloy via correlation functions and stochastic material reconstruction*. Acta Materialia, 2013. **61**(9): p. 3370-3377.
85. Guo, E.-Y., N. Chawla, T. Jing, S. Torquato, and Y. Jiao, *Accurate modeling and reconstruction of three-dimensional percolating filamentary microstructures from two-dimensional micrographs via dilation-erosion method*. Materials Characterization, 2014. **89**: p. 33-42.
86. Jiao, Y. and N. Chawla, *Three dimensional modeling of complex heterogeneous materials via statistical microstructural descriptors*. Integrating Materials and Manufacturing Innovation, 2014. **3**(1): p. 1-19.
87. Jiao, Y. and N. Chawla, *Modeling and characterizing anisotropic inclusion orientation in heterogeneous material via directional cluster functions and stochastic microstructure reconstruction*. Journal of Applied Physics, 2014. **115**(9): p. 093511.
88. Chen, S., H. Li, and Y. Jiao, *Dynamic reconstruction of heterogeneous materials and microstructure evolution*. Physical Review E, 2015. **92**(2): p. 023301.
89. Chen, S., A. Kirubanandham, N. Chawla, and Y. Jiao, *Stochastic Multi-Scale Reconstruction of 3D Microstructure Consisting of Polycrystalline Grains and Second-Phase Particles from 2D Micrographs*. Metallurgical and Materials Transactions A, 2016. **47**: p. 1-11.
90. Li, H., S. Singh, N. Chawla, and Y. Jiao, *Direct Extraction of Spatial Correlation Functions from Limited X-ray Tomography Data for Microstructure Quantification*. in preparation, 2016.
91. Li, H., P.-E. Chen, and Y. Jiao, *Accurate Reconstruction of Porous Materials via Stochastic Fusion of Limited Bimodal Microstructural Data*. Transport in Porous Media, 2017: p. 1-18.
92. Gommès, C., Y. Jiao, and S. Torquato, *Density of states for a specified correlation function and the energy landscape*. Physical review letters, 2012. **108**(8): p. 080601.
93. Gommès, C.J., Y. Jiao, and S. Torquato, *Microstructural degeneracy associated with a two-point correlation function and its information content*. Physical Review E, 2012. **85**(5): p. 051140.
94. Jiao, Y., F. Stillinger, and S. Torquato, *Geometrical ambiguity of pair statistics: Point configurations*. Physical Review E, 2010. **81**(1): p. 011105.

95. Jiao, Y., F.H. Stillinger, and S. Torquato, *Geometrical ambiguity of pair statistics. II. Heterogeneous media*. Physical Review E, 2010. **82**(1): p. 011106.
96. Torquato, S., J. Beasley, and Y. Chiew, *Two-point cluster function for continuum percolation*. The Journal of chemical physics, 1988. **88**(10): p. 6540-6547.
97. Cinlar, E. and S. Torquato, *Exact determination of the two-point cluster function for one-dimensional continuum percolation*. Journal of statistical physics, 1995. **78**(3-4): p. 827-839.
98. Prager, S., *Interphase transfer in stationary two-phase media*. Chemical Engineering Science, 1963. **18**(4): p. 227-231.
99. Torquato, S., *Interfacial surface statistics arising in diffusion and flow problems in porous media*. The Journal of chemical physics, 1986. **85**(8): p. 4622-4628.
100. Chen, P.-E., W. Xu, N. Chawla, Y. Ren, and Y. Jiao, *Hierarchical n-point polytope functions for quantitative representation of complex heterogeneous materials and microstructural evolution*. Acta Materialia, 2019. **179**: p. 317-327.
101. Torquato, S. and Y. Jiao, *Dense packings of the Platonic and Archimedean solids*. Nature, 2009. **460**(7257): p. 876.
102. Yeong, C. and S. Torquato, *Reconstructing random media*. Physical Review E, 1998. **57**(1): p. 495.
103. Yeong, C. and S. Torquato, *Reconstructing random media. II. Three-dimensional media from two-dimensional cuts*. Physical Review E, 1998. **58**(1): p. 224.
104. Kirkpatrick, S., C.D. Gelatt, and M.P. Vecchi, *Optimization by simulated annealing*. science, 1983. **220**(4598): p. 671-680.
105. Hwang, C.-R., *Simulated annealing: theory and applications*. Acta Applicandae Mathematicae, 1988. **12**(1): p. 108-111.
106. Gommers, C.J., Y. Jiao, A.P. Roberts, and D. Jeulin, *Chord-length distributions cannot generally be obtained from small-angle scattering*. Journal of Applied Crystallography, 2020. **53**(1).
107. Torquato, S. and Y. Jiao, *Effect of dimensionality on the continuum percolation of overlapping hyperspheres and hypercubes. II. Simulation results and analyses*. The Journal of chemical physics, 2012. **137**(7): p. 074106.
108. Sahimi, M., *Applications of percolation theory*. 1994: CRC Press.
109. Cang, R., H. Li, H. Yao, Y. Jiao, and Y. Ren, *Improving direct physical properties prediction of heterogeneous materials from imaging data via convolutional neural network and a morphology-aware generative model*. Computational Materials Science, 2018. **150**: p. 212-221.
110. Cang, R., Y. Xu, S. Chen, Y. Liu, Y. Jiao, and M.Y. Ren, *Microstructure Representation and Reconstruction of Heterogeneous Materials via Deep Belief Network for Computational Material Design*. Journal of Mechanical Design, 2017. **139**(7): p. 071404.
111. Kamrava, S., P. Tahmasebi, and M. Sahimi, *Linking morphology of porous media to their macroscopic permeability by deep learning*. Transport in Porous Media, 2020. **131**(2): p. 427-448.